Nanoscale

Accepted Manuscript

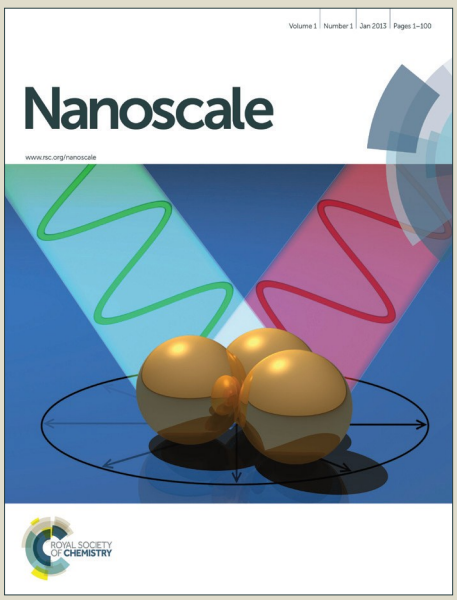

ROYAL SOCIETY OF CHEMISTRY

www.rsc.org/nanoscale

Journal Name

ARTICLE

CVD synthesis of $Mo_{(1-x)}W_xS_2$ and $MoS_{2(1-x)}Se_{2x}$ alloy monolayers aimed at tuning the bandgap of molybdenum disulfide

Received 00th January 20xx,
Accepted 00th January 20xx

DOI: 10.1039/x0xx00000x

www.rsc.org/

Wenting Zhang,[a] Xiaodong Li,[a] Tongtong Jiang,[a] Jiangluqi Song,[a] Yue Lin,[b] Lixin Zhu*[c] and Xiaoliang Xu*[a]

As a rising star in two-dimensional (2D) layered materials, transition metal dichalcogenides (TMDs) have attracted tremendous attention for their potential applications in nanoelectronics, optoelectronics and photonics. Driven by the high standards of practical devices, alloying theory has been proposed for modulating electronic structure of TMDs materials as well as their physical and chemical properties. So far, however, very limited alloy materials can be synthesized by chemical vapor deposition (CVD) and very limited band gap range can be achieved. Here, for the first time, we report a one-step CVD strategy for the growth of ternary alloy $Mo_{(1-x)}W_xS_2$ monolayers (ML) on SiO_2/Si substrates with controllable composition. Both $Mo_{(1-x)}W_xS_2$ and $MoS_{2(1-x)}Se_{2x}$ alloy materials with high crystallinity were synthesized in this work. Therefore, the bandgap photoluminescence (PL) can be broadening from 1.97 eV (for ML-WS_2) to 1.55 eV (for ML-$MoSe_2$). Further, the density functional theory calculations were performed to reveal the important role of alloying in tailoring the electronic structure of 2D materials.

Introduction

Undoubtedly, graphene synthesized experimentally for the first time in 2004 has brought the dramatic revolution to the field of materials and condensed matter.[1-4] With the deeper and broader research about it,[5-7] some other novel two-dimensional (2D) materials have aroused the great interest of the researchers, due to their special physical and chemistry properties, peculiar structures and anticipated potential applications. The typical representative of these thriving 2D materials including the insulating hexagonal boron nitride (h-BN) which can provide an atomically flat surface and has proven to be the best substrate materials.[8, 9] In addition, the semiconductor transition metal dichalcogenides (TMDs) whose band gap depends on the thickness also host excellent mechanical properties similar to graphene. In some degree, the emergence of these ultrathin 2D layered materials has complemented the zero band gap shortcomings of graphene which has seriously retarded its application in digital circuits and low-power electronics.[10] Especially in the rich library of TMDs, different members such as WS_2 ~2.0 eV,[11] WSe_2~1.65 eV,[12] MoS_2 ~1.8 eV,[13, 14] $MoSe_2$ ~1.55 eV,[15-17] $MoTe_2$ ~1.0 eV,[18] and WTe_2 ~1.0 eV,[19] always possess different direct band gap when their thickness thinning down to the monolayer (ML). Benefit from this character, they are expected to be the promising candidate for building the atomically thin layered devices such as field-effect transistors,[20-22] optical sensors and some other (opto-)electronics.[23-25]

So far, considerable efforts have been dedicated to the preparation and application of ML-TMDs materials. It is widely believed that a major opportunity for TMDs and their more versatile applications lie in the tunability of band gap continuously.[26-31] Before this, alloying materials with different band gap is an important strategy in the band gap engineering of bulk semiconductors and 0D/1D nanomaterials. So, taking into account the similarities in atomic structure and properties of the TMDs family members (MX_2: M = Mo, W; X = S, Se, Te), it is possible to create a mixed alloy system with a tunable band gap and not suffer from phase separation.[32-37] Recently, the large-area monolayers MoS_2/$MoSe_2$/WS_2/WSe_2 have been synthesized by the chemical vapor deposition (CVD).[38-45] The scale of the monolayer film even reaches the centimeter length. Thus suggests that CVD is the most efficient method to synthesize the binary ML-TMDs with practical applied val-

[a] Key Laboratory of Strongly-Coupled Quantum Matter Physics, Chinese Academy of Sciences, School of Physical Sciences, University of Science and Technology of China, Hefei, Anhui, 230026, P. R. China. Email: xlxu@ustc.edu.cn.
[b] Hefei National Laboratory for Physical Sciences at the Microscale, University of Science and Technology of China, Hefei, Anhui, 230026, P. R. China.
[c] Center Laboratory, First Affiliated Hospital of Anhui Medical University, Hefei, Anhui, 230026, P. R. China. E-mail: lx-zhu@163.com.
† Electronic Supplementary Information (ESI) available: TEM images, EDX spectrums, Raman spectroscopy and intensity 2D mappings of alloy samples. See DOI: 10.1039/x0xx00000x

unlike the bad reproducibility and low throughput of the traditional mechanical/chemical exfoliation or hydrothermal synthesis.[46-49] However, as far as we know, ML-$MoS_{2(1-x)}Se_{2x}$ is the only ternary alloys synthesized successfully by CVD to date, which means the band gap of TMDs can only be tuned between 1.55 eV (ML-$MoSe_2$) and 1.8 eV (ML-MoS_2) arbitrarily. In order to incorporate TMDs into more rational applications, it is imperative to further broaden the tunable range of TMDs by CVD.

In this study, the high-quality ternary alloy of ML-$Mo_{(1-x)}W_xS_2$ was synthesized by one-step CVD process for the first time. Both Raman and photoluminescence (PL) spectra, as well as the transmission electron microscopy (TEM) indicated that these achieved ML-$Mo_{(1-x)}W_xS_2$ are of high crystalline quality and remarkable PL emission as good as the mechanical exfoliation samples.[27, 34] The band gap of ML-$Mo_{(1-x)}W_xS_2$ could be tuned precisely between 1.83 eV (ML-MoS_2) and 1.97 eV (ML-WS_2) by changing the ratio of Mo/W compositions. Combining with the ML-$MoS_{2(1-x)}Se_{2x}$, the final tunable range of TMDs band gap was broaden from 1.55 eV (ML- $MoSe_2$) to 1.97 eV by CVD synthesis.

Experimental section

Synthesis of $Mo_{(1-x)}W_xS_2$ monolayers: The home-built CVD system was used to synthesize the ternary alloy ML-$Mo_{(1-x)}W_xS_2$, Fig. 1a gives the schematic representation. The whole process took place in a quartz tube using a dual-zone horizontal tubular furnace to control the supply rates of chalcogenide and metal source independently. The quartz boat loaded with sulfur fine powder (99.5%) was placed in the center of first heating zone, while another boat loaded with a mixture of MoO_3 (99.99%) and WO_3(99.99%) powder was placed in the second heating zone at downstream. The growth substrate (a Si substrate covered with a 285 nm SiO_2 layer) was positioned directly on top of it. The distance between two quartz boats was about 20 cm which had been demonstrated to be a suitable distance. Before heating, the tube was pumped down to the lowest attainable pressures in the system (about 100 mTorr), then ultrahigh purity argon gas (99.99%) was introduced to remove oxygen residue and some other sources of contamination from air. The two heating zones of furnace were then heated to the certain temperature within 30 min (750 ^{o}C for the mixture of MoO_3 and WO_3, 150 ^{o}C for S), keeping the raw materials under the respective constant temperature for about 15 min, followed by natural cooling down. The flow rate of Ar during the whole growth process was set to 25 sccm.

Synthesis of $MoS_{2(1-x)}Se_{2x}$ monolayers: As for ML-$MoS_{2(1-x)}Se_{2x}$, the mixed powder of S and Se (99.99%) were used as source of chalcogenide combined with MoO_3 as sole metal source. Moreover, considering the different melting points of materials, the growth temperature changed to 680 ^{o}C for MoO_3 and 280 ^{o}C for the mixture of S and Se powder, while the other experimental parameters remain the same.

Characterization

Optical microscopy (OM, Leica DM4000M) was used to make a preliminary judgment about the location, shape and layer number of the prepared samples. Then the scanning electron microscope (SEM, JSM-6700F) was used to further characterize the microstructures and morphologies. Atomic force microscopy (AFM, SPA-300HV &SPI3800N) gave the more accurate information about the thickness and surface roughness of the samples. Transmission electron microscope (TEM, JEOL JEM-ARM200F) was used directly to identify the crystal structure and quality, which was operated at an acceleration voltage of 200 kV. Finally, both Raman and PL measurements were performed on LabRAM HR800 under ambient condition at room temperature, the excitation source was an Ar-ion laser with wavelength centered at 532 nm and the power was 2 mW so that no observable samples heating.

Results and discussion

In this work, both the ternary alloy of ML-$Mo_{(1-x)}W_xS_2$ and ML-$MoS_{2(1-x)}Se_{2x}$ were successfully synthesized with tunable compositions by CVD. Compared with the traditional mechanical exfoliating method, this simple CVD synthesis could effectively reduce the surface contamination. The final crystal structure of the as-synthesized alloy samples is similar to ML-MoS_2 described in Fig. 1(b). Here, a hexagonal metal-plane containing Mo (W) atoms surrounded above and below by planes of chalcogen atoms (S/Se) in displaced hexagonal sites. Thanks to the isomorphism of MX_2 (MoS_2/$MoSe_2$/WS_2), the hexagonal lattices structure did not be disturbed obviously by the introduction of doping elements.

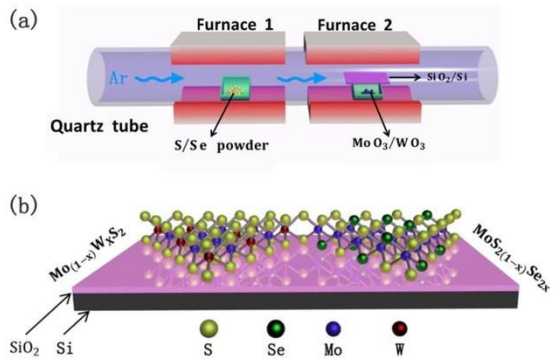

Fig.1 (a) Schematic of the tube-furnace set-up employed in this work for the growth of ternary alloy monolayers. (b) Schematic diagram of the two-dimensional structures of ML-$Mo_{(1-x)}W_xS_2$ (left) and ML-$MoS_{2(1-x)}Se_{2x}$ (right) respectively.

The Optical microscopy (OM) images of the as-prepared ML-$Mo_{(1-x)}W_xS_2$ and ML-$MoS_{2(1-x)}Se_{2x}$ are given in Fig. 2(a) and (b). It provided one of the most intuitive approaches to identify

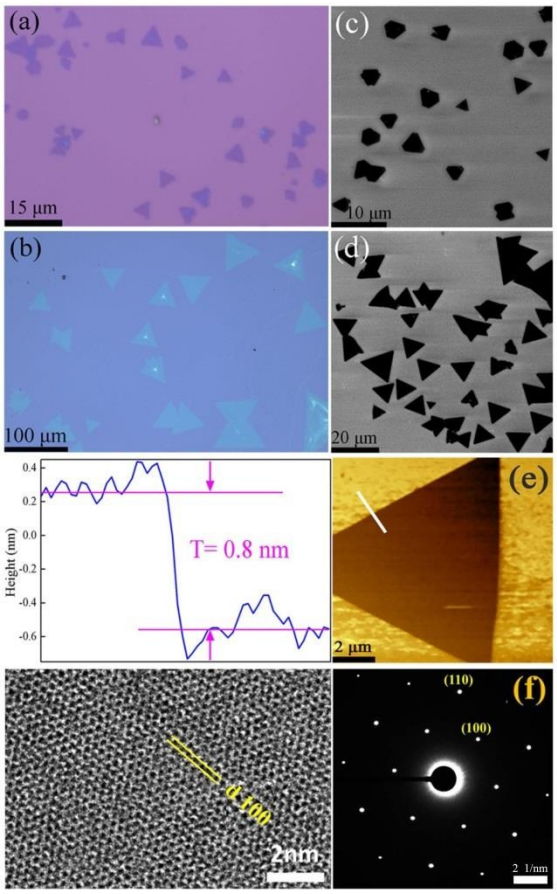

Fig.2 (a)-(b) Typical optical images of the obtained ternary ML-$Mo_{(1-x)}W_xS_2$ and ML-$MoS_{2(1-x)}Se_{2x}$ respectively. (c)-(d) SEM morphology of the corresponding ML-$Mo_{(1-x)}W_xS_2$ and ML-$MoS_{2(1-x)}Se_{2x}$. (e) AFM height topography of an ML-$MoS_{2(1-x)}Se_{2x}$ triangle and the height profile showed the thickness of~0.8 nm, as measured along the white line. (f) HRTEM image taken from an ML-$Mo_{(1-x)}W_xS_2$ nanonsheet and the corresponding SAED pattern which showing only one set of six-fold symmetry diffraction spots.

the number of layers, based on the thickness dependent contrast which can distinguish between the single- and multi-layers on 285 nm SiO_2 /Si. As Fig. 2(a) and (b) show, these achieved triangular nanosheets with the edge lengths ranging from a few to dozens of microns. The bright nucleation sites and thicker area in some triangles are noticeable similar to what has been observed in the growth of pristine MoS_2.[39, 44] Fig. 2(c) and (d) are the typical scanning electron microscopy (SEM) images. The remarkable chiaroscuro between samples and substrate indicates that they nucleate randomly on the substrate, and most of them are the isolated islands with triangle-like morphologies which can be understood based on the presence of an energetically preferred edge, i.e., the zigzag edge.[45] One of typical $MoS_{2(1-x)}Se_{2x}$ triangles was selected to perform atomic force microscopy (AFM) in order to make sure the domains imaged by OM were monolayer. The line scan in Fig. 2(e) indicates that the thickness is ~0.8 nm which is comparable to the previous reports about exfoliated monolayer samples.[27] The homogeneous color contrast in AFM image indicates that the flake has flat and uniform surface without any observable large scale absorbents or multilayer growth. Furthermore, in order to identify the crystallinity of these nanosheets, we used a combination of TEM and electron diffraction techniques. The monolayer samples were first transferred onto TEM microgrids using a PMMA-assisted transfer technology, the dark-field image of a ML-$Mo_{(1-x)}W_xS_2$ nanosheet supported on holey carbon grid is given in supporting information Fig. S1†. Fig. 2(f) shows the corresponding high-resolution TEM (HRTEM) image of the nanosheet, which with a lattice fringe of 0.28nm, in accordance with the (100) lattice plane. The selected area electron diffraction (SAED) pattern presents only one set of six-fold symmetry diffraction spots (right in Fig. 3(f)), further confirming the high single-crystallinity with hexagonal structure of these achieved ML-$Mo_{(1-x)}W_xS_2$ nanosheets. Besides, to unambiguously determine the chemical modulation of the samples, we performed elemental analysis using energy dispersive X-ray spectroscopy (EDS) equipped TEM. Both the EDX spectrum and elemental mapping images of the typical $Mo_{(1-x)}W_xS_2$ nanosheet are given in Fig. S2†. The results corroborated that the sample consisted of Mo, W, and S elements, with the W mole fraction [x, W/(W+Mo)] of~0.1, indicating the composition of the nanosheet as $Mo_{0.9}W_{0.1}S_2$. Additionally, the detailed analysis about the microstructure and elemental composition of the ML-$MoS_{2(1-x)}Se_{2x}$ nanosheets are also given in Fig. S3†-4†, from which the similar conclusion can be deduced.

We then use Raman spectroscopy to characterize the composition-dependent vibration modes of these alloy monolayers, as shown in Fig. 3(a). Previously studies have indicated that two kinds of characteristic Raman vibration modes always can be found in 2D metal dichalcogenide, i.e. the out-of-plane vibration mode (A mode) and the in-plane vibration mode (E mode). In our case, the molecular vibration modes of ternary alloy ML-$Mo_{(1-x)}W_xS_2$ and ML-$MoS_{2(1-x)}Se_{2x}$ can be classified into two sets, to which one set related the MoS_2-like modes and the other related the WS_2-like (or $MoSe_2$-like). The curves a-e in Fig. 3(a) describe the vibrational behavior of composition modulated ML-$Mo_{(1-x)}W_xS_2$ alloys with the x decreased gradually from 1 (pure WS_2) to 0 (pure MoS_2). Different from the "two-mode behavior" (2MB) of $MoS_{2(x-1)}Se_{2x}$ alloys,[31] there is little difference between frequencies of phonon modes in the pure MoS_2 and WS_2 (less than 50 cm^{-1}). So the MoS_2-like and WS_2-like A_{1g} (E_{2g}^1) shifted closer to each other and then partially overlap. The two identifiable peaks appeared in 355.5 cm^{-1} and 420.5 cm^{-1} can be assigned to the WS_2-like E_{2g}^1 and A_{1g} mode respectively. While the other two peaks near 384 cm^{-1} and 404 cm^{-1} belong to the MoS_2-like E_{2g}^1 and A_{1g} mode. As expected, the Raman spectrum of ML-$Mo_{(1-x)}W_xS_2$ changed with W content obviously. The MoS_2-like A_{1g} and E_{2g}^1 modes in alloys shifted to higher and lower energies respectively with increasing W content, leading to the larger peak separation (~24cm^{-1}) than that of the pure binary compound ML-MoS_2 (~20 cm^{-1}) (the local amplification of this area can be found in supporting information Fig. S5†). While the WS_2-like A_{1g} and E_{2g}^1 modes shifted to lower and hig

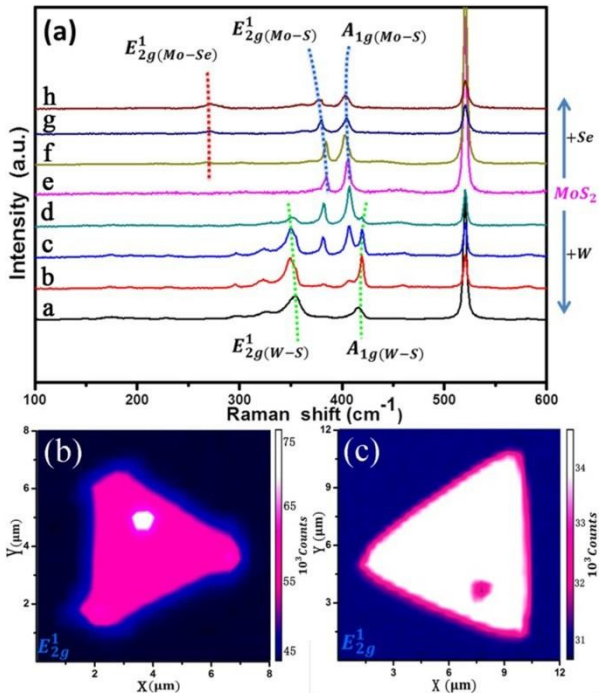

Fig.3 (a) Raman spectrum of the ML-$Mo_{(1-x)}W_xS_2$ and ML-$MoS_{2(1-x)}Se_{2x}$ nanosheets excited with a 532 nm argon ion laser, the dotted lines indicate the change of the peak position correspondingly. (b)-(c) Raman peak intensity mapping at the WS_2-like and $MoSe_2$-like $E_{2g}{}^1$ mode respectively.

energies respectively and come close to the corresponding modes of pure binary compound ML-WS_2 gradually, just as the green dashed line depicted in Fig. 3(a). By investigating the possible factors that contribute to stiffen or soften the different vibration modes, three factors are particularly notable for the phenomenon. First, the doped and host atoms have different atomic weight (W atom is 1.92 times heavier than Mo).[32] This mass difference may directly cause the change of vibration energy. Second, the size difference between the two metal atoms would change the length of the chemical bond. It has been reported that the bond length in atomically thin WS_2 (~0.2401 nm) is shorter than that in atomically thin MoS_2 (~0.2417 nm).[50] This may impact the bond energy or even induce the local strain in system, all of which would result in the movement of Raman peaks. Third, two kinds of atoms possess the different electron affinity (W~ 0.8163 eV, Mo~ 0.7473 eV).[37] It is directly related to the change of molecular polarizability, which is considered to be the key factor influencing the Raman signal. Therefore, the above synchronous changes of physical and chemical properties are predominantly responsible for this phenomenon. Compared with the slight movement of peak position (less than 4 cm^{-1}) in Raman spectrum, the change of relative intensity is more obvious. Along with the gradual increase of W content (from curves e to a), the relative intensity of WS_2-like modes has experienced the obvious change from the weak to strong. While, the change tendency of MoS_2-like modes is just the reverse of it. The emergence of this phenomenon is physically expected since that the Raman peak intensity is always proportional to the amount of substance under the same test conditions. This furti indicates that the feature of WS_2 in the ternary alloy is mor and more dominant with the increase of W doping.

In other side, the curves f-h in Fig. 3(a) give the Raman information about ML-$MoS_{2(1-x)}Se_{2x}$ with the increase of S content. For the $MoSe_2$-like modes, the $E_{2g}{}^1$ mode locating at low frequencies ~272 cm^{-1} is absent or too weak to recogniz at the initial stage, and then gradually come into appearance with the corresponding intensity increased. The other MoSe like A_{1g} mode is too weak to distinguish in our case. What's more, with the Se content increasing, the relative intensity of MoS_2-like A_{1g} and $E_{2g}{}^1$ modes both decreased along with the peak position gradually moving down. This opposite chang tendency of the relative intensity within $MoSe_2$-like and MoS_2 like modes indicated the successful incorporation of S content, which also agrees with the EDX characterization (Fig S4†). The moving tendency of the peak position with increase of Se content was depicted by the red and blue dashed lines in Fig. 3(a). The interactions between S and atoms combined with the effects mentioned above are considered to contribute to soften the S–Mo related mod and decrease their vibration frequency. This behavior consistent with the earlier reports.[35]

Comparing the Raman signal of two kinds of alloy materials the relatively stronger WS_2-like modes than $MoSe_2$-like may h due to the high alloying degree between W and Mo atoms.[33] Also, it is worth to emphasize again, in all of our ML-Mo$_{(1-x)}W_xS_2$ alloy samples, both the MoS_2-like and WS_2-like vibration modes are clear enough to be identified especially the tw prominent first-order Raman-active modes A_{1g} and $E_{2g}{}^1$. However, for the samples obtained by mechanic exfoliating,[27, 32, 34] the Raman spectrum is only dominated by three vibration mode peaks which may be caused by th serious overlap effect. From this we can speculate that both the nature of two parent binary compound MoS_2 and WS_2 c be effectively kept. They also can friendly coexist without serious interfere with each other in alloy samples. This could be the main improvement of the samples synthesized by CVD which may allow for more opportunities to further optimiz the performance of photoelectric device or some other fie Furthermore, we select the WS_2-like $E_{2g}{}^1$ mode at ~355.5 cm^{-1} and $MoSe_2$-like $E_{2g}{}^1$ mode at ~272 cm^{-1} to plot the Rama intensity 2D mappings of ML-$Mo_{(1-x)}W_xS_2$ and ML-$MoS_{2(1-x)}Se$ respectively. As seen in Fig. 3(b) and (c), the intensity of tw triangle domains showed the absence of obvious fluctuation. suggests that our samples possess the high homogeneity an crystal quality without the noteworthy phase segregation. Th mappings of other modes are also given in supportin information (Fig. S6†), which further confirmed the implementation of high quality alloy materials. From th foregoing, the vibrational behavior of alloys is seen to be more complex than that of the stoichiometric compounds, and mor research needed to be devoted to understand the Raman characterization.

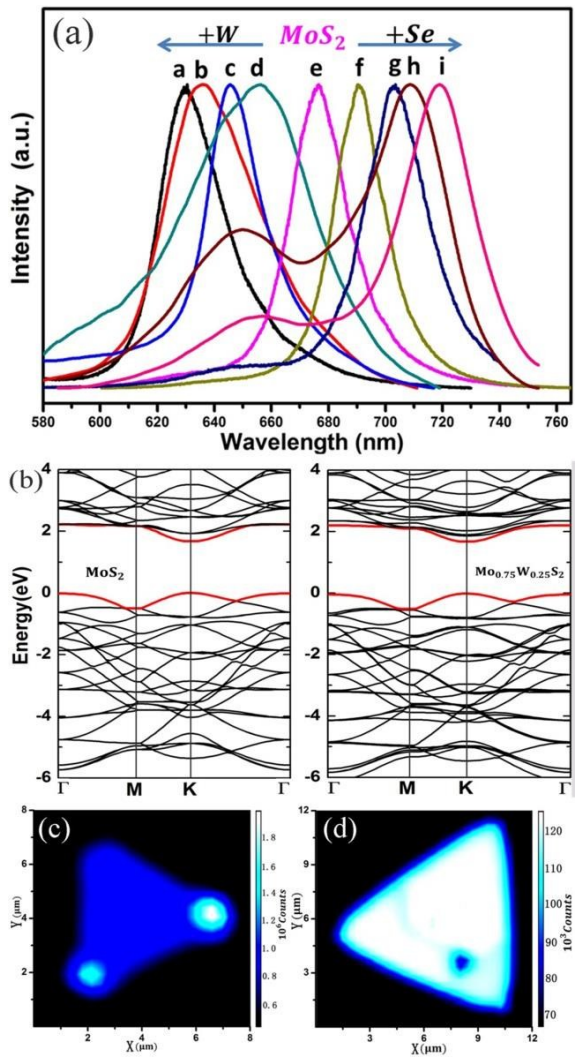

Fig.4 (a) Composition-dependent PL spectra of the ML-$Mo_{(1-x)}W_xS_2$ and ML-$MoS_{2(1-x)}Se_{2x}$ excited with a 532 nm argon ion laser. The PL intensity is normalized by the maximum emission intensity (i.e., intensity of A exciton emission). (b) DFT-calculated band structure of ML-MoS_2 (left) and ML-$Mo_{(1-x)}W_xS_2$ (right) with x=0.25 .The direct gap is located at K point for both of them. (c)-(d) Typical PL mappings of the single ternary nanosheet of ML-$Mo_{(1-x)}W_xS_2$ and ML-$MoS_{2(1-x)}Se_{2x}$ respectively

Indisputably, Micro-PL spectroscopy is one of the most effective methods for determining the optical band gap of 2D materials. Here it was used to examine the modification of the optical band gap which was a function of component in ternary alloy monolayers. Fig. 4(a) gives the PL spectrum of these two kinds of alloys simultaneously. One prominent peak correspond to A exaciton (low energy one) emissions, another broad peak located at short wave region correspond to B exaciton (high energy one) emissions which has relative weak intensity. These band-edge excitonic transitions attribute to the valence splitting affected by the giant spin-orbit coupling,[15] which is also a strong evidence of their direct bandgap properties. With the increase of W composition (form curves d to a in Fig. 4(a)), the PL emission peak blue shift constantly until the upper limit of ~630 nm (~1.97 eV) for pure WS_2. On the contrary, the introduction of Se (form curves e to i in Fig. 4(a)) made the PL emission red shift continuously starting from ~676nm (~1.83 eV) for pure MoS_2. Both the Se and W components in the adjustment role of optical band gap is obvious in the PL measurement.

To get insight into the composition-dependent electronic structure of alloy monolayers, the ML-$Mo_{(1-x)}W_xS_2$ was chosen to perform the density functional theory (DFT) calculations using the Vienna ab initio simulation package (VASP).[27, 36] The projected augmented-wave pseudopotentials and the exchange-correlation functional of Perdew, Burke and Ernzerhof (PBE) were employed.[20, 51] We constructed a single-layer MoS_2 supercell to be the calculated model, and then substituted 25% Mo atoms by W atoms randomly. The choice of the final structure based on whether the correlation functions were close to that of a random alloy, so that the physical properties of the truly random alloy can be well simulated. The calculated electronic band structures of ML-$Mo_{0.75}W_{0.25}S_2$, together with that of pure ML-MoS_2 are shown in Fig. 4(b). The DFT calculations indeed show that the defect-free MoS_2 has a direct bandgap of 1.672 eV which is in accordance with the earlier DFT calculations.[52] While, the direct bandgap of ML-$Mo_{0.75}W_{0.25}S_2$ is 1.686 eV with well-defined the conduction band minimum (CBM) and valence band maximum (VBM) both located at the K point. Although the calculated bandgaps vary only by 0.14 eV, it proved that the bandgap would be increased toward that of WS_2 with the small amount of W incorporating into MoS_2. The trend in bandgap variation with the component content matches well with the experimental observed PL spectrum in Fig. 4(a). The above results demonstrated that alloying approach is effective to extend the range of band gaps, which will be beneficial for optoelectronic applications.

PL mapping on the corresponding triangles in Fig. 3(b) and (c) were also performed by plotting the 2D spatial distribution of the PL center energy. The images were measured by stepping a focused excitation laser (532 nm) across the samples and integrating the PL signal from each point, as shown in Fig. 4(c) and (d). Two ternary alloy monolayers with a certain W or Se concentration both showed the uniform light emission across the whole microstructure, and virtually no compositional fluctuations related large spatial variation can be discerned. From above all, optical studies demonstrated again the high crystallinity and excellent optical properties of the synthesized ML-$Mo_{(1-x)}W_xS_2$ and ML-$MoS_{2(1-x)}Se_{2x}$, which were consistent with the other characterization results of structural and composition in the preceding text.

Conclusions

In summary, a simple one-step chemical vapor deposition (CVD) approach was successfully used to synthesize ternary alloy $Mo_{(1-x)}W_xS_2$ (for the first time) and $MoS_{2(1-x)}Se_{2x}$ with excellent uniformity and controllable composition. The microstructure, thickness and crystallinity of the as-grown samples were measured by OM, SEM AFM and TEM, confirming that most of triangular single-crystals are monolayers. Then Raman and PL

spectroscopy were used to analyze the characteristic peak shifts, showing a high degree of homogeneity and stability of the alloy samples against phase separation. Also, from Raman signal, the CVD-synthesized ML-$Mo_{(1-x)}W_xS_2$ was speculated to be able to better retain the characteristics of the parent materials than generated by mechanical exfoliating. More importantly, both the experiments and theoretical simulations showed that these 2D ternary alloys remain the direct bandgap semiconductors with high photoluminescence intensity. The optical bandgap values can be broaden to the range of 1.97 eV~1.55 eV through controlling the ratio of Mo/W or S/Se in precursors. The effective implementation of bandgap engineering in these atomically thin 2D nanostructures is of great significance to further optimize the performance of nanoscale photoelectric devices, such as the sensitivity, response rate and so on.

Acknowledgements

We sincerely acknowledge financial support from the National Natural Science Foundation of China (No. 51272246, 11404314) and Scientific and Technological Research Foundation of Anhui (No. 12010202035).

References

1 K. S. Novoselov, A. K. Geim, S. V. Morozov, D. Jiang, Y. Zhang, S. V. Dubonos, I. V. Grigorieva and A. A. Firsov, *Science*, 2004, 306, 666-669.
2 D. Haberer, D. V. Vyalikh, S. Taioli, B. Dora, M. Farjam, J. Fink, D. Marchenko, T. Pichler, K. Ziegler, S. Simonucci, M. S. Dresselhaus, M. Knupfer, B. Buchner and A. Gruneis, *Nano letters*, 2010, 10, 3360-3366.
3 Z. H. Ni, T. Yu, Y. H. Lu, Y. Y. Wang, Y. P. Feng and Z. X. Shen, *Acs Nano*, 2008, 2, 2301-2305.
4 B. Y. Dai, L. Fu, Z. Y. Zou, M. Wang, H. T. Xu, S. Wang and Z. F. Liu, *Nature Communications*, 2011, 2.
5 X. Huang, Z. Y. Yin, S. X. Wu, X. Y. Qi, Q. Y. He, Q. C. Zhang, Q. Y. Yan, F. Boey and H. Zhang, *Small*, 2011, 7, 1876-1902.
6 Z. Liu, L. L. Ma, G. Shi, W. Zhou, Y. J. Gong, S. D. Lei, X. B. Yang, J. N. Zhang, J. J. Yu, K. P. Hackenberg, A. Babakhani, J. C. Idrobo, R. Vajtai, J. Lou and P. M. Ajayan, *Nature nanotechnology*, 2013, 8, 119-124.
7 Y. J. Gong, G. Shi, Z. H. Zhang, W. Zhou, J. Jung, W. L. Gao, L. L. Ma, Y. Yang, S. B. Yang, G. You, R. Vajtai, Q. F. Xu, A. H. MacDonald, B. I. Yakobson, J. Lou, Z. Liu and P. M. Ajayan, *Nature Communications*, 2014, 5.
8 C. R. Dean, A. F. Young, I. Meric, C. Lee, L. Wang, S. Sorgenfrei, K. Watanabe, T. Taniguchi, P. Kim, K. L. Shepard and J. Hone, *Nature nanotechnology*, 2010, 5, 722-726.
9 M. Okada, T. Sawazaki, K. Watanabe, T. Taniguch, H. Hibino, H. Shinohara and R. Kitaura, *Acs Nano*, 2014, 8, 8273-8277.
10 F. Schwierz, *P Ieee*, 2013, 101, 1567-1584.
11 H. R. Gutierrez, N. Perea-Lopez, A. L. Elias, A. Berkdemir, B. Wang, R. Lv, F. Lopez-Urias, V. H. Crespi, H. Terrones and M. Terrones, *Nano letters*, 2013, 13, 3447-3454.
12 W. Zhao, Z. Ghorannevis, K. K. Amara, J. R. Pang, M. Toh, X. Zhang, C. Kloc, P. H. Tan and G. Eda, *Nanoscale*, 2013, 5, 9677-9683.
13 N. Liu, P. Kim, J. H. Kim, J. H. Ye, S. Kim and C. J. Lee, *Acs Nano*, 2014, 8, 6902-6910.
14 A. Gurarslan, Y. F. Yu, L. Q. Su, Y. L. Yu, F. Suarez, S. Yao, Y. Zhu, M. Ozturk, Y. Zhang and L. Y. Cao, *Acs Nano*, 2014, 8, 11522-11528.
15 G. W. Shim, K. Yoo, S. B. Seo, J. Shin, D. Y. Jung, I. S. Kang, C. W. Ahn, B. J. Cho and S. Y. Choi, *Acs Nano*, 2014, 8, 6655-6662.
16 J. C. Shaw, H. L. Zhou, Y. Chen, N. O. Weiss, Y. Liu, Y. Huang and X. F. Duan, *Nano Research*, 2014, 7, 511-517.
17 X. L. Wang, Y. J. Gong, G. Shi, W. L. Chow, K. Keyshar, G. L. Ye, R. Vajtai, J. Lou, Z. Liu, E. Ringe, B. K. Tay and P. M. Ajayan, *Acs Nano*, 2014, 8, 5125-5131.
18 S. Balendhran, S. Walia, H. Nili, J. Z. Ou, S. Zhuiykov, R. B. Kaner, S. Sriram, M. Bhaskaran and K. Kalantar-zadeh, *Advanced Functional Materials*, 2013, 23, 3952-3970.
19 Y. Ding, Y. L. Wang, J. Ni, L. Shi, S. Q. Shi and W. H. Tang, *Physica B*, 2011, 406, 2254-2260.
20 J. Kang, S. Tongay, J. Zhou, J. Li and J. Wu, *Applied Physics Letters*, 2013, 102, 012111.
21 G. H. Lee, Y. J. Yu, X. Cui, N. Petrone, C. H. Lee, M. S. Choi, D. Y. Lee, C. Lee, W. J. Yoo, K. Watanabe, T. Taniguchi, C. Nuckolls, P. Kim and J. Hone, *Acs Nano*, 2013, 7, 7931-7936.
22 A. K. Geim and I. V. Grigorieva, *Nature*, 2013, 499, 419-425.
23 S. Tongay, J. Suh, C. Ataca, W. Fan, A. Luce, J. S. Kang, J. Liu, C. Ko, R. Raghunathanan, J. Zhou, F. Ogletree, J. Li, J. C. Grossman and J. Wu, *Scientific reports*, 2013, 3, 2657.
24 R. Cheng, D. Li, H. Zhou, C. Wang, A. Yin, S. Jiang, Y. Liu, Y. Chen, Y. Huang and X. Duan, *Nano letters*, 2014, 14, 5590-5597.
25 J. Xia, X. Huang, L. Z. Liu, M. Wang, L. Wang, B. Huang, D. D. Zhu, J. J. Li, C. Z. Gu and X. M. Meng, *Nanoscale*, 2014, 6, 8949-8955.
26 Q. Ma, M. Isarraraz, C. S. Wang, E. Preciado, V. Klee, S. Bobek, K. Yamaguchi, E. Li, P. M. Odenthal, A. Nguyen, D. Barroso, D. Z. Sun, G. V. Palacio, M. Gomez, A. Nguyen, D. Le, G. Pawin, J. Mann, T. F. Heinz, T. S. Rahman and L. Bartels, *Acs Nano*, 2014, 8, 4672-4677.
27 Y. F. Chen, J. Y. Xi, D. O. Dumcenco, Z. Liu, K. Suenaga, D. Wang, Z. G. Shuai, Y. S. Huang and L. M. Xie, *Acs Nano*, 2013, 7, 4610-4616.
28 K. Xu, F. M. Wang, Z. X. Wang, X. Y. Zhan, Q. S. Wang, Z. Z. Cheng, M. Safdar and J. He, *Acs Nano*, 2014, 8, 8468-8476.
29 S. Tongay, J. Zhou, C. Ataca, J. Liu, J. S. Kang, T. S. Matthews, L. You, J. Li, J. C. Grossman and J. Wu, *Nano letters*, 2013, 13, 2831-2836.
30 Y. Gong, Z. Liu, A. R. Lupini, G. Shi, J. Lin, S. Najmaei, Z. Lin, A. L. Elias, A. Berkdemir, G. You, H. Terrones, M. Terrones, R. Vajtai, S. T. Pantelides, S. J. Pennycook, J. Lou, W. Zhou and P. M. Ajayan, *Nano letters*, 2014, 14, 442-449.
31 J. Mann, Q. Ma, P. M. Odenthal, M. Isarraraz, D. Le, E. Preciado, D. Barroso, K. Yamaguchi, G. von Son Palacio, A. Nguyen, T. Tran, M. Wurch, A. Nguyen, V. Klee, S. Bobek, D. Sun, T. F. Heinz, T. S. Rahman, R. Kawakami and L. Bartels, *Advanced materials*, 2014, 26, 1399-1404.
32 D. O. Dumcenco, K. Y. Chen, Y. P. Wang, Y. S. Huang and K. K. Tiong, *Journal of Alloys and Compounds*, 2010, 506, 940-943.
33 D. O. Dumcenco, H. Kobayashi, Z. Liu, Y. S. Huang and K. Suenaga, *Nat Commun*, 2013, 4, 1351.
34 Y. Chen, D. O. Dumcenco, Y. Zhu, X. Zhang, N. Mao, Q. Feng, M. Zhang, J. Zhang, P. H. Tan, Y. S. Huang and L. Xie, *Nanoscale*, 2014, 6, 2833-2839.
35 H. Li, X. Duan, X. Wu, X. Zhuang, H. Zhou, Q. Zhang, X. Zhu, W. Hu, P. Ren, P. Guo, L. Ma, X. Fan, X. Wang, J. Xu, A. Pan and X. Duan, *Journal of the American Chemical Society*, 2014, 136, 3756-3759.
36 S. Tongay, D. S. Narang, J. Kang, W. Fan, C. Ko, A. V. Luce, K. X. Wang, J. Suh, K. D. Patel, V. M. Pathak, J. Li and J. Wu, *Applied Physics Letters*, 2014, 104, 012101.

37 H. Liu, K. K. Antwi, S. Chua and D. Chi, *Nanoscale*, 2014, 6, 624-629.
38 S. Najmaei, Z. Liu, W. Zhou, X. Zou, G. Shi, S. Lei, B. I. Yakobson, J. C. Idrobo, P. M. Ajayan and J. Lou, *Nature materials*, 2013, 12, 754-759.
39 A. M. van der Zande, P. Y. Huang, D. A. Chenet, T. C. Berkelbach, Y. You, G. H. Lee, T. F. Heinz, D. R. Reichman, D. A. Muller and J. C. Hone, *Nature materials*, 2013, 12, 554-561.
40 Y. Yu, C. Li, Y. Liu, L. Su, Y. Zhang and L. Cao, *Scientific reports*, 2013, 3, 1866.
41 X. Duan, C. Wang, J. C. Shaw, R. Cheng, Y. Chen, H. Li, X. Wu, Y. Tang, Q. Zhang, A. Pan, J. Jiang, R. Yu, Y. Huang and X. Duan, *Nature nanotechnology*, 2014, 9, 1024-1030.
42 Y. Gong, J. Lin, X. Wang, G. Shi, S. Lei, Z. Lin, X. Zou, G. Ye, R. Vajtai, B. I. Yakobson, H. Terrones, M. Terrones, B. K. Tay, J. Lou, S. T. Pantelides, Z. Liu, W. Zhou and P. M. Ajayan, *Nature materials*, 2014, 13, 1135-1142.
43 C. Huang, S. Wu, A. M. Sanchez, J. J. Peters, R. Beanland, J. S. Ross, P. Rivera, W. Yao, D. H. Cobden and X. Xu, *Nature materials*, 2014, 13, 1096-1101.
44 Z. Liu, M. Amani, S. Najmaei, Q. Xu, X. Zou, W. Zhou, T. Yu, C. Qiu, A. G. Birdwell, F. J. Crowne, R. Vajtai, B. I. Yakobson, Z. Xia, M. Dubey, P. M. Ajayan and J. Lou, *Nat Commun*, 2014, 5, 5246.
45 S. Wang, Y. Rong, Y. Fan, M. Pacios, H. Bhaskaran, K. He and J. H. Warner, *Chemistry of Materials*, 2014, 26, 6371-6379.
46 W. Y. Yin, L. Yan, J. Yu, G. Tian, L. J. Zhou, X. P. Zheng, X. Zhang, Y. Yong, J. Li, Z. J. Gu and Y. L. Zhao, *Acs Nano*, 2014, 8, 6922-6933.
47 Y. C. Wang, J. Z. Ou, S. Balendhran, A. F. Chrimes, M. Mortazavi, D. D. Yao, M. R. Field, K. Latham, V. Bansal, J. R. Friend, S. Zhuiykov, N. V. Medhekar, M. S. Strano and K. Kalantar-zadeh, *Acs Nano*, 2013, 7, 10083-10093.
48 K. K. Liu, W. Zhang, Y. H. Lee, Y. C. Lin, M. T. Chang, C. Y. Su, C. S. Chang, H. Li, Y. Shi, H. Zhang, C. S. Lai and L. J. Li, *Nano letters*, 2012, 12, 1538-1544.
49 X. Lu, M. I. Utama, J. Zhang, Y. Zhao and Q. Xiong, *Nanoscale*, 2013, 5, 8904-8908.
50 H. Terrones, F. Lopez-Urias and M. Terrones, *Scientific reports*, 2013, 3.
51 J. Kang, S. Tongay, J. Li and J. Wu, *Journal of Applied Physics*, 2013, 113, 143703.
52 H. Qiu, T. Xu, Z. Wang, W. Ren, H. Nan, Z. Ni, Q. Chen, S. Yuan, F. Miao, F. Song, G. Long, Y. Shi, L. Sun, J. Wang and X. Wang, *Nat Commun*, 2013, 4, 2642.